Remote Sensing of Environment 271 (2022) 112894

Contents lists available at ScienceDirect

Remote Sensing of Environment

journal homepage: www.elsevier.com/locate/rse

Mapping land subsidence and aquifer system properties of the Willcox Basin, Arizona, from InSAR observations and independent component analysis

Mimi Peng [a,b], Zhong Lu [c,*], Chaoying Zhao [a,e], Mahdi Motagh [b,d], Lin Bai [a,e], Brian D. Conway [f], Hengyi Chen [a]

[a] School of Geological Engineering and Geomatics, Chang'an University, Xi'an 710054, China
[b] Helmholtz Centre Potsdam, GFZ German Research Centre for Geosciences, Department of Geodesy, Section of Remote Sensing and Geoinformatics, Potsdam 14473, Germany
[c] Roy M. Huffington Department of Earth Sciences, Southern Methodist University, Dallas, TX 75275, USA
[d] Institute of Photogrammetry and Geo-Information, Leibniz University Hannover, Hannover 30167, Germany
[e] Key Laboratory of Western China's Mineral Resources and Geological Engineering, Ministry of Education, Xi'an 710054, China
[f] Arizona Department of Water Resources, 1110 W. Washington St, Suite 310, Phoenix, AZ 85012, USA

ARTICLE INFO

Editor: Jing M. Chen

Keywords:
InSAR
Aquifer system
Hydraulic head
Willcox Basin
Independent component analysis

ABSTRACT

Long-term excessive groundwater exploitation for agricultural, domestic and stock applications has resulted in substantial ground subsidence in Arizona, USA, and especially in the Willcox Groundwater Basin. The land subsidence rate of the Willcox Basin has not declined but has rather increased in recent years, posing a threat to infrastructure, aquifer systems, and ecological environments. In this study, we first investigate the spatiotemporal characteristics of land subsidence in the Willcox Groundwater Basin using an interferometric synthetic aperture radar (InSAR) time series analytical approach with L-band ALOS and C-band Sentinel-1 SAR data acquired from 2006 to 2020. The overall deformation patterns are characterized by two major zones of subsidence, with the mean subsidence rate increasing with time from 2006 to 2020. An approach based on independent component analysis (ICA) was adopted to separate the mixed InSAR time series signal into a set of independent signals. The application of ICA to the Willcox Basin not only revealed that two different spatiotemporal deformation features exist in the basin but also filtered the residual errors in InSAR observations to enhance the deformation time series. Integrating the InSAR deformation and groundwater level data, the response of the aquifer skeletal system to the change in hydraulic head was quantified, and the hydromechanical properties of the aquifer system were characterized. Historical spatiotemporal storage loss from 1990 to 2020 was also estimated using InSAR measurements, hydraulic head and estimated skeletal storativity. Understanding the characteristics of land surface deformation and quantifying the response of aquifer systems in the Willcox Basin and other groundwater basins elsewhere are important in managing groundwater exploitation to sustain the mechanical health and integrity of aquifer systems.

1. Introduction

Land subsidence induced by excessive exploitation of groundwater resources is an environmental geohazard that affects many agricultural and urban areas in the world, such as Xi'an, Beijing and the Yellow River Delta in China (Peng et al., 2019, 2020; Chen et al., 2020; Liu et al., 2021); California's Central Valley and Houston in the USA (Gualandi and Liu, 2021; Qu et al., 2015); Mexico City (Cigna and Tapete, 2021); and Tehran, Iran (Haghshenas-Haghighi and Motagh, 2019). Overdrafting of groundwater resources disrupts the normal periodic groundwater balance held in aquifer systems, causing a reduction in pore pressure and an increase in effective stress. The susceptible aquifer skeleton and clay deposits may then consolidate or compact, leading to surface subsidence by the rearrangement of the grains due to the stress change in the confined aquifer system (Terzaghi, 1925, 1943). Consequences associated with ground subsidence include damage to

* Corresponding author.
E-mail address: zhonglu@smu.edu (Z. Lu).

https://doi.org/10.1016/j.rse.2022.112894
Received 18 July 2021; Received in revised form 29 December 2021; Accepted 4 January 2022

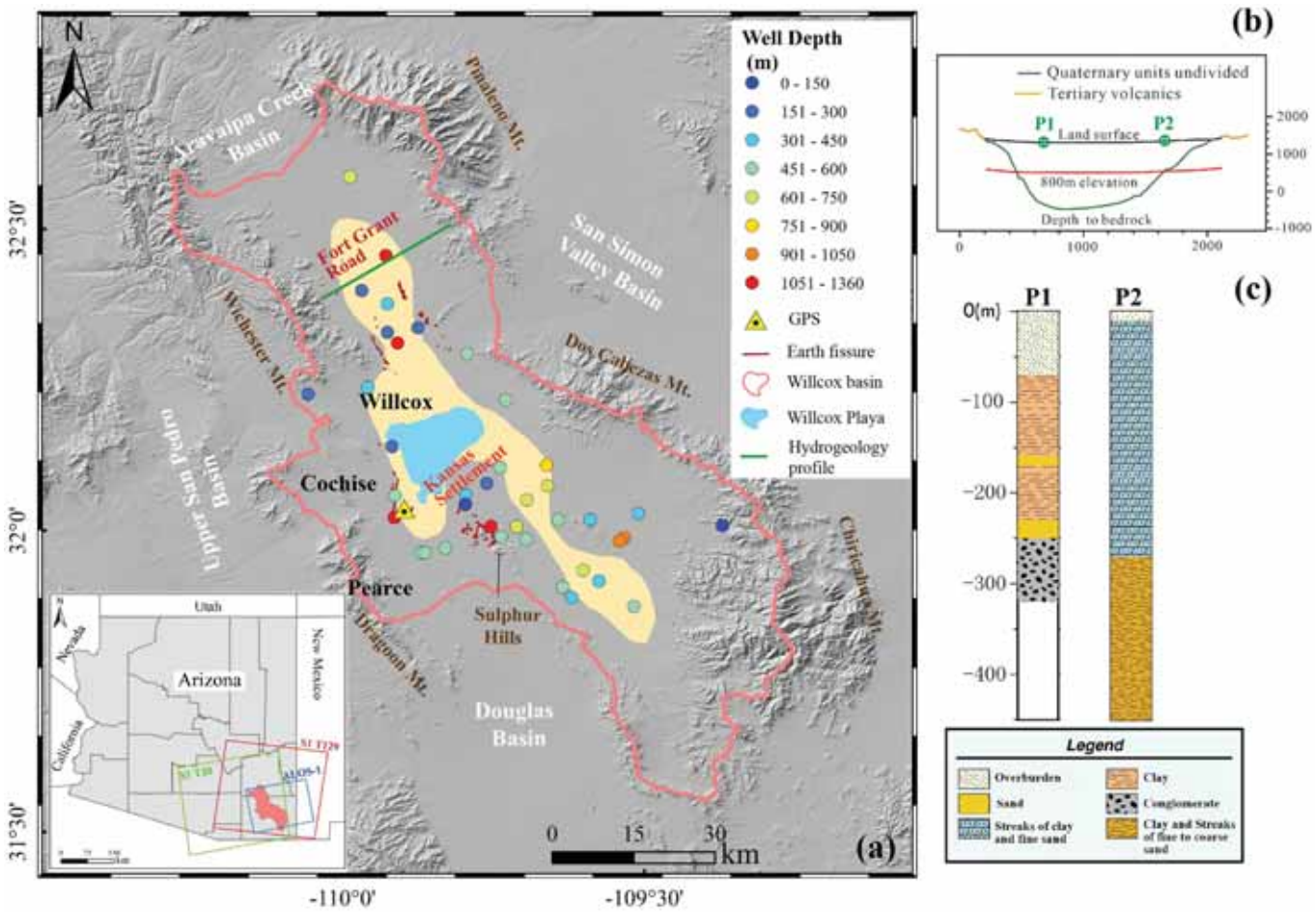

Fig. 1. (a) Location and extent of the Willcox Basin. The pink line represents the basin boundary. The location and drilling depth of wells are indicated by coloured dots. The yellow triangle is the location of a GPS station. The yellow area indicates the area where sediment thickness reaches more than 800 m. The short red lines represent earth fissures that are composed of many small segments. The inset in the bottom-left corner shows a brief overview of the study area within Arizona, and the SAR satellite footprints are indicated by polygons with different colours. (b) Simple geologic cross-section along the green profile in (a). (c) Hydrogeological columns with an approximate depth at P1 and P2. (For interpretation of the references to colour in this figure legend, the reader is referred to the web version of this article.)

infrastructure, roads and buildings, formation of earth fissures, and increased exposure to flooding and salinization of land in coastal areas (Peng et al., 2019, 2020; Blackwell et al., 2020). Furthermore, land subsidence may indicate the land surface response of permanent compaction of an aquifer system (Fetter, 2000), which can lead to a reduction in aquifer storage capacity and groundwater stock.

Hydrological storage properties characterize the capacity of an aquifer system to store and release groundwater. Normally, these physical properties are determined by a combination of field sampling and laboratory testing on aquifer material samples, which can be time-consuming and effort-intensive (Fetter, 2000). However, studies have shown that ground surface deformation can be an indirect measurement of aquifer compaction, which could be combined with groundwater level recordings to quantify aquifer properties as well as storage capacity and to evaluate the consequences of groundwater depletion on a stressed aquifer system (Amelung et al., 1999; Lu and Danskin, 2001).

Interferometric synthetic aperture radar (InSAR) has been established as one of the most cost-effective techniques for measuring ground surface deformation over large areas at a fine spatial resolution of metres and with centimetre-level accuracy under favourable conditions. InSAR is becoming an increasingly popular and effective geodetic technique for mapping aquifer system compaction in groundwater basins and probing the hydrological parameters of the underlying aquifer systems in conjunction with groundwater level data (Chaussard et al., 2014; Gualandi and Liu, 2021; Jiang et al., 2018; Miller and Shirzaei, 2015; Miller et al., 2017; Motagh et al., 2017).

From the early 1900s onwards, Arizona has been experiencing significant land subsidence (Conway, 2016; Miller and Shirzaei, 2015; Miller et al., 2017). The Willcox Groundwater Basin has the largest ground subsidence rate in Arizona (ADWR, 2015b). Due to groundwater pumping far exceeding the natural mountain front recharge, groundwater levels will likely continue to decline, resulting in continued land subsidence (Conway, 2016). The basin currently does not have any external sources of surface water that could supplement groundwater use and slow this decline. There is a long-term imbalance between aquifer inflow and outflow. It is estimated that current groundwater production exceeds recharge by a factor of three to eight in the basin (Conway, 2016). Long-term subsidence has led to subsidence-related earth fissures in the basin, damaging infrastructure, such as buildings, highways, roads, flood-control structures, gas lines, and water and sewer lines.

Signal separation techniques, such as principal component analysis (PCA) and independent component analysis (ICA), have been introduced to the InSAR field to isolate geophysical signals of interest. PCA is a technique to extract uncorrelated signals embedded in mixed data and then concentrate them within a few principal components (PCs). In other words, it is used to reduce data dimensionality. Earlier studies have applied PCA to invert geodetic observations for temporal variations

in fault slip and magmatic inflation (Kositsky and Avouac, 2010; Lin et al., 2010), to reduce InSAR displacement time series noise (Chen et al., 2019) and to identify sinkhole and ground motions with different characteristics (Bonì et al., 2016; Vajedian and Motagh, 2019). ICA is a leading method for blind source separation to isolate signals without knowing a priori information about the signal sources (Hyvärinen and Oja, 2000; Ghosh et al., 2021). Unlike PCA, ICA primarily attempts to decompose the multivariate signal into a set of statistically independent components (ICs). ICA has been successfully used for error estimation and separation in InSAR data processing (Liang et al., 2019; Maubant et al., 2020), landslide mechanism analysis (Cohen-Waeber et al., 2018), and hydrogeology (Chaussard and Farr, 2019; Chaussard et al., 2017).

Measuring surface deformation associated with groundwater exploitation and understanding the responses of the aquifer system to changes in groundwater are needed for managing groundwater resources and controlling land subsidence. Therefore, in this study, the spatiotemporal evolution of multidimensional deformation with high accuracy is derived using the multitemporal InSAR method and ICA. After signal separation, different deformation patterns and their mechanisms are also revealed. Furthermore, aquifer parameters and groundwater storage (GWS) variations of the confined aquifer system in the Willcox Basin are quantified by using the InSAR technique as well as hydraulic head data.

2. Study area and datasets

2.1. Willcox Basin

The Willcox Basin, located in southeastern Arizona, covers an area of approximately 4950 km^2 and is essentially a closed broad alluvial valley basin. The mountainous area of the Willcox Basin covers approximately 1450 km^2, and the valley floor covers approximately 3500 km^2. The basin measures approximately 15 km to 45 km in width and is 160 km long (Gootee, 2012). The basin is bounded by the Aravaipa Creek Basin to the north, the San Simon Valley Subbasin to the east, the Douglas Basin to the south, and the Upper San Pedro Basin to the west (Fig. 1).

The Willcox Playa, located in the centre of the basin, is a large, irregularly shaped alkali flat with approximately 130 km^2 of almost no vegetation. The playa is a remnant of Pleistocene-age Lake Cochise (Oram, 1993) and overlies the deepest part of the basin. Most surface water and groundwater in the regional aquifer flows towards the low-lying playa area in the closed basin.

In regard to the hydrological setting, the basin-fill materials are generally composed of alluvial, lacustrine and volcanic rocks (Oram, 1993). The floor and sides of the Willcox Basin consist of impermeable igneous, metamorphic and sedimentary rocks that crop out in the surrounding mountains. Saturated basin-fill deposits underlie much of the valley floor and compose the regional aquifer system. The depth to bedrock in the Willcox Basin increases from zero at the basin margins to over 1220 m below the land surface in the deeper, central portion of the basin (Fig. 1). This basin's principal water-bearing unit is an alluvial aquifer that consists of unconsolidated strata and lacustrine deposits. Aquifer materials in the Fort Grant Road (FGR hereinafter) district are more permeable but much less homogeneous than those in the Kansas Settlement (KS hereinafter) district (Towne and Freark, 2001; Richard et al., 2000). The northern FGR district and southern KS district are the major agricultural regions, where the majority of groundwater is pumped for irrigation.

2.2. SAR interferometric datasets

In this study, C-band Sentinel-1 and L-band ALOS-1 SAR datasets were jointly used to investigate the land deformation across the Willcox Groundwater Basin. Fig. 1 illustrates the footprints and flight directions of different SAR tracks. Two stacks of 117 and 88 Sentinel-1 SAR scenes spanning from 2015 to 2020 were acquired in descending mode along track T129 and in ascending mode along track T20, respectively. Fourteen SAR acquisitions from the ALOS-1 sensor were acquired from 2006 to 2011. The detailed parameters of the SAR datasets are listed in Table 1.

Table 1
List of different SAR datasets used in this study.

	Sentinel-1		ALOS-1
	T129	T20	
Band/wavelength (cm)	C/5.6	C/5.6	L/23.6
Incidence angle (°)	39.3	43.9	38.7
Orbit direction	Descending	Ascending	Ascending
Acquisition dates	2015-11-26 - 2020-07-14	2016-10-08 - 2020-06-19	2006-12-06 - 2011-02-01
Total acquisitions	117	88	14

2.3. Hydraulic head and GPS data

Arizona legislation in 1980 authorized the Arizona Department of Water Resources (ADWR) to manage and regulate groundwater exploitation to minimize overexploitation to eliminate overdrafts by 2025. The ADWR Groundwater Site Inventory (GWSI) provides information related to well location, well status, and groundwater measurements (ADWR, 2015a).

In the Willcox Basin, a total of 48 groundwater monitoring wells that were sampled more than once in the observation period were used to estimate the aquifer parameters. Hydraulic head observations were recorded once per year around November. Of the 48 available observation wells, there are 39 wells with recorded drilling depths ranging from 100 to 1356 m, which means that the exploitation of groundwater occurs in deep confined aquifers (Fig. 1).

Only one GPS benchmark provided by the ADWR is available in the study area. The GPS benchmark has been surveyed a few times a year since 2016, providing in situ measurements with an accuracy of a few centimetres (https://geodesy.noaa.gov/) (Fig. 1).

3. Methodology

Fig. 2 illustrates the major data-processing flow and steps utilized in this study, and details on the methods are presented as follows.

3.1. InSAR time series processing

Spatiotemporal land deformation measurements over each SAR data track were derived using the small baseline subset (SBAS) InSAR approach based on GAMMA software (Berardino et al., 2002; Lanari et al., 2004; Werner et al., 2000). Ascending and descending InSAR measurements were integrated using the multidimensional small BAseline subset (MSBAS) method to estimate vertical and east-west deformation time series over overlapping regions and were combined with their temporal resolution (Samsonov and d'Oreye, 2017).

Sentinel-1 TOPS data require a very high coregistration accuracy ($\sim 10^{-3}$ pixels) to prevent the phase ramp caused by the Doppler centroid shift (De Zan and Monti Guarnieri, 2006). We applied multilooking factors of 4 by 1 and 2 by 4 (range and azimuth, respectively) for the Sentinel-1 and ALOS-1 datasets, respectively, to lower speckle noise in the interferograms. The spatial samplings of interferograms were ~ 15 m. Based on the coherence quality, a total of 157 interferograms were generated from data stack T129, 149 from T20, and 33 from ALOS-1. Then, the topographic phase component from each interferogram was removed using a one-arc-second (~30 m) digital elevation model obtained freely from the Shuttle Radar Topography Mission (SRTM).

After phase unwrapping using the extended minimum cost flow algorithm (Werner et al., 2000), a linear model was used to remove the

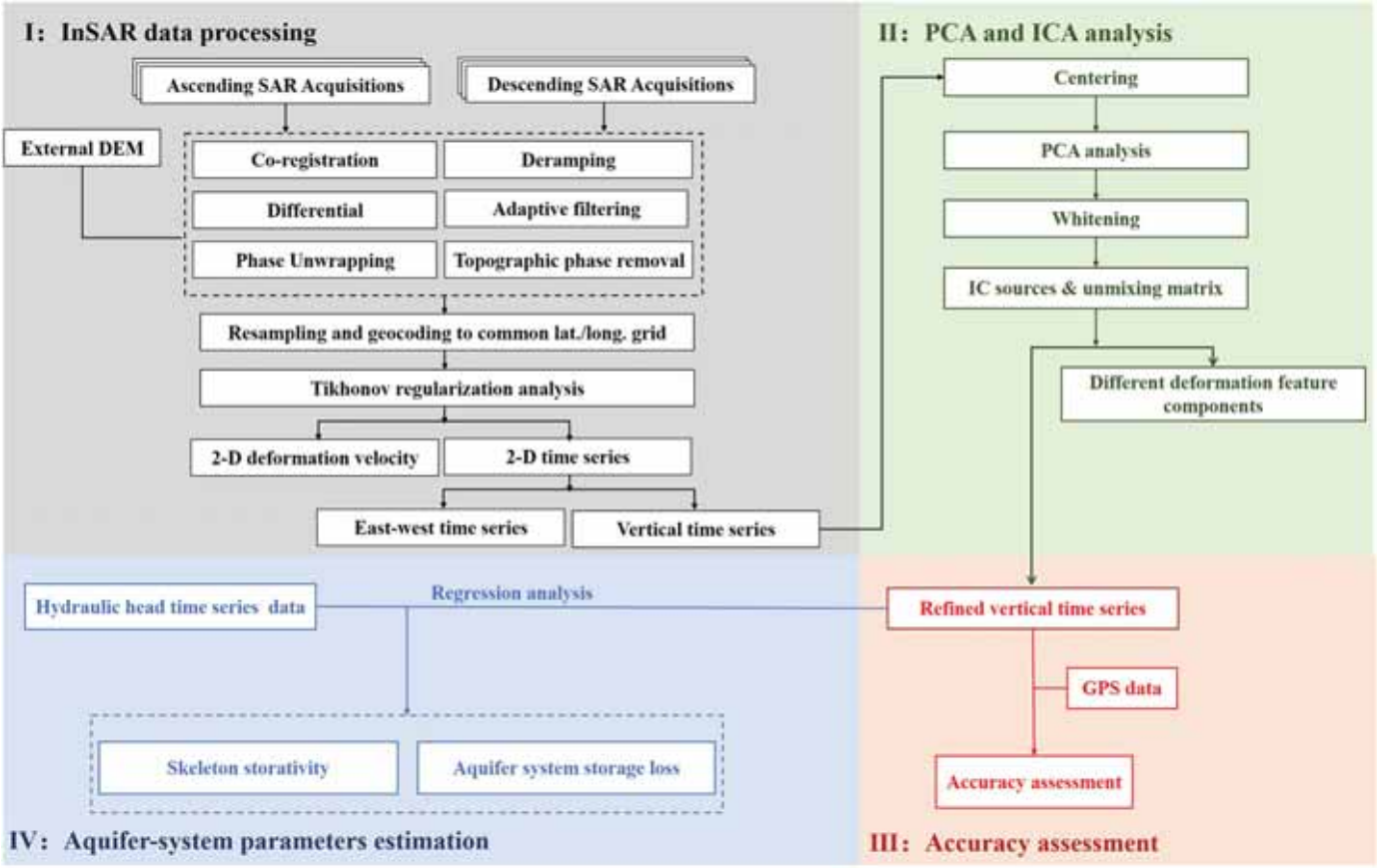

Fig. 2. Flowchart of data processing.

elevation-dependent phase component in every interferogram, and the phase ramp was separated with a quadratic model. Finally, the phase average velocity and time series at coherent targets along line-of-sight (LOS) were retrieved by stacking and least squares solutions.

3.2. ICA decomposition

ICA, as a computational signal separation method, effectively decomposes a mixed signal into a set of linear combinations of statistically independent signal sources. After multitemporal InSAR inversion, the InSAR time series signal can be decomposed into several latent signal sources without considering any a priori information. This is achieved under the assumption that each independent component follows a non-Gaussian probability distribution. The relationship between the observed mixed signals and independent sources is simply formulated as:

$$O_{t\times n} = D_{t\times l}\bullet \mathrm{S}_{\mathrm{l}\times \mathrm{n}} \tag{1}$$

where O is the matrix of observed InSAR time series; D is described as a mixing matrix; each column of the matrix corresponds to the coefficients of the relative contribution of each independent source; S is the decomposed source matrix of the original observation matrix; each row corresponds to an independent source; l is the number of independent components; t is the number of SAR acquisitions; and the pixel number at each acquisition is n. In this study, the ICA approach deployed was the fast fixed-point algorithm for ICA (FastICA) (Hyvärinen, 1999).

This algorithm begins by whitening the observations and centering them to produce an orthogonal mixing matrix. We centred the observations by subtracting the mean from the mixed signal matrix so that they became zero-mean variables. FastICA enabled the centred observations by preconditioning them with PCA, which could be used as an additional way of reducing data dimensionality and noise. Afterwards, the mixed signals were linearly transformed to be expressed as uncorrelated variables with variance equal to 1 by whitening. The mixed matrix preprocessed by centering and whitening was represented by W. The problem thus turned to $W = \widehat{D}\bullet \mathrm{S}$, where $\widehat{D}$ is the orthogonally adjusted mixing matrix. Then, the source matrix can be estimated by equation $S = \widehat{D}^{-1}\bullet \mathrm{W}$, where $\widehat{D}^{-1}$ is called the unmixing matrix U. Afterwards, a fixed-point iteration algorithm built into FastICA was utilized by maximizing spatial non-Gaussian sources to derive the source matrix (S), mixing matrix and unmixing matrix (U).

3.3. Estimation of aquifer mechanical properties

The long-term groundwater depletion across the Willcox Basin has caused the water table to decline to the deep confined aquifer, and no compaction deformation is expected in the upper unconfined aquifer. In addition, soil moisture-induced transient surface deformation (Molan and Lu, 2020) is negligible for long-term groundwater analysis. The relationship between the observed land subsidence variations and the hydraulic head changes in a confined aquifer is in accordance with the principle of effective stress and hydromechanical consolidation theory (Galloway and Burbey, 2011; Terzaghi, 1925). Specific storage (S_s) of a confined aquifer is the amount of water per unit volume of a saturated formation that is stored or expelled from storage due to the compressibility of the aquifer system and the pore water per unit change in water head, which is given by the following expression (Fetter, 2000; Jacob, 1950).

$$S_s = \rho_w g(\alpha + n\beta) \tag{2}$$

where ρ_w is the water density, g is the gravitational acceleration, α is the

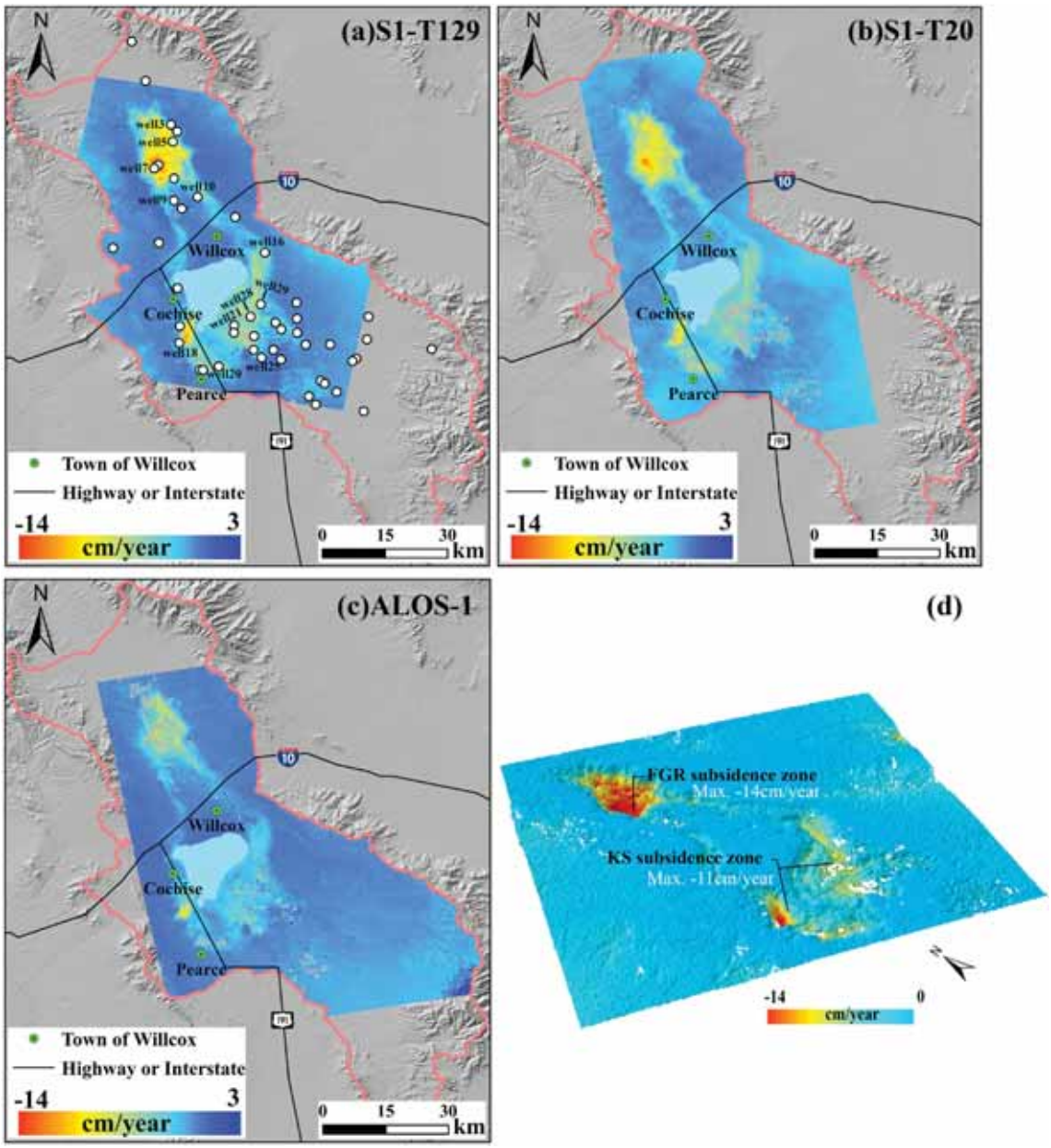

Fig. 3. Maps of the average deformation rate in the LOS direction across the Willcox Basin derived from (a) descending Sentinel-1 T129 spanning from 2015 to 2020, (b) ascending Sentinel-1 T20 spanning from 2016 to 2020, and (c) ALOS-1 data spanning from 2006 to 2011. The white dots in (a) indicate the locations of 48 available observation wells. (d) 3-D display of the deformation velocity map (a).

aquifer compressibility, n is the porosity and β is the water compressibility. Specific storage has a dimension of $1/L$. S_s is composed of skeletal compressibility S_k and water compressibility S_w: $S_s = S_k + S_w$. In general, in compacting aquifers, water compressibility S_w is much smaller than skeletal compressibility S_k. Consequently, it is assumed to be negligible (Chaussard et al., 2014; Fetter, 2000; Hoffmann et al., 2003).

The total stress σ is defined as the sum of the effective stress σ' and pore pressure p. Normally, the total stress in the confined aquifer remains constant under natural conditions or a constant overburden load. Then, the change in effective stress σ' controls land subsidence or uplift. Hence, $\Delta\rho = -\Delta\sigma' = \Delta h\rho_w g$, where Δh denotes the change in hydraulic head. An increase in effective stress corresponds to the compaction of multiple aquifer materials, regardless of low-permeability clays or high-permeability gravels and sands. Then, aquifer compressibility is expressed as

$$\alpha = \frac{-\Delta b}{\Delta\sigma' b_o} = \frac{\Delta b}{\Delta h \rho_w g b_o} \tag{3}$$

where Δb and b_o represent the compaction amount and the initial thickness of the aquifer system, respectively (Jacob, 1950).

3.3.1. Estimation of skeletal storage coefficients

Incorporating Eq. (2) with Eq. (3), the dimensionless skeletal storage coefficient (S_{sk}) is defined as:

$$S_{sk} = S_k b_o = \frac{\Delta b}{\Delta h} \tag{4}$$

The storage coefficient, also storativity, is the volume of water that a permeable unit absorbs or releases from storage per unit surface area per unit change in head. Skeletal storativity S_{sk} can be characterized as a combination of elastic (S_{ske}) and inelastic (S_{skv}) skeletal storativity,

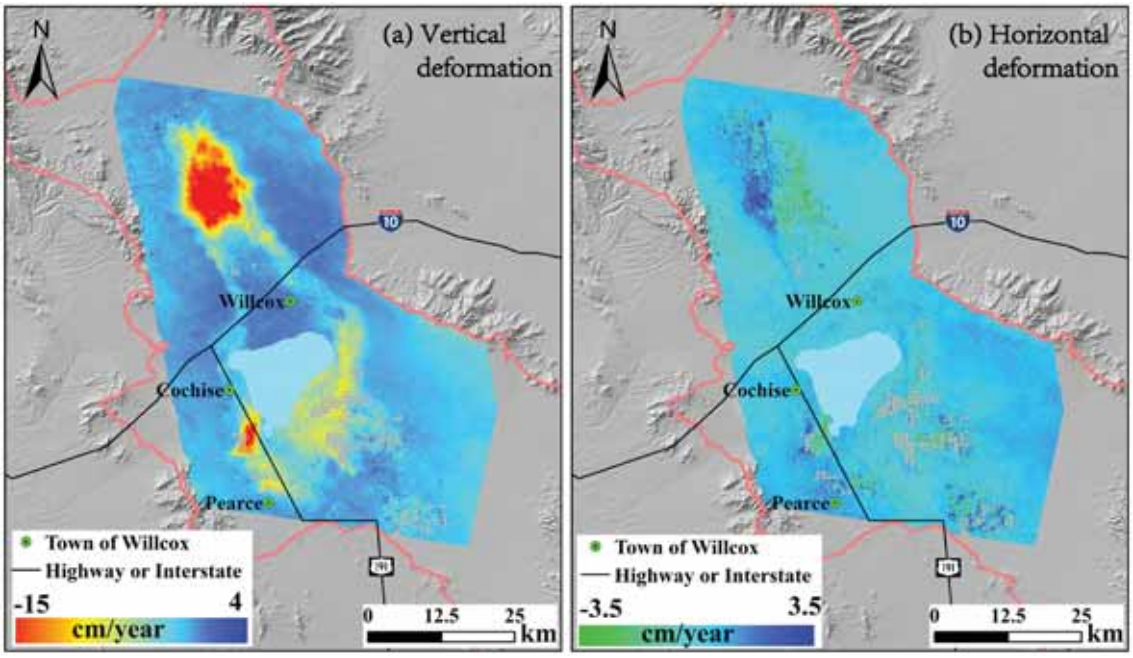

Fig. 4. 2-dimensional average deformation map during 2016–2020 estimated from ascending and descending Sentinel SAR data: (a) the vertical component; and (b) the horizontal (east-west) component.

depending on whether the skeletal effective stress is greater than the preconsolidation stress (σ_{max}') or the hydraulic head is lower than the previous lowest water level (Galloway and Burbey, 2011; Hoffmann et al., 2003). Here, the preconsolidation stress refers to the maximum effective stress of an aquifer in the past.

$$S_{sk} = \begin{cases} S_{ske} = \dfrac{\Delta b_s}{\Delta h_s} & for\ \ \acute{\sigma} < \acute{\sigma}_{max} \\ S_{skv} = \dfrac{\Delta b_v}{\Delta h_v} & for\ \ \acute{\sigma} \geq \acute{\sigma}_{max} \end{cases} \tag{5}$$

where Δb_s and Δh_s represent the elastic/seasonal changes in the vertical displacement component and hydraulic head time series, respectively. Δb_v and Δh_v represent the inelastic/long-term compaction amount and hydraulic head drop, respectively. Elastic skeletal storage characterizes the fluid volume increase/reduction as the groundwater level fluctuates over an aquifer system, which corresponds to the elastic and recoverable deformation on the surface. In contrast, inelastic skeletal storage characterizes the long-term compaction and decrease in fluid volume as the head drops, which corresponds to irreversible and inelastic deformation of the aquifer system. Normally, the inelastic skeletal storage coefficient can be larger than the elastic coefficient by several orders of magnitude (Fetter, 2000). Permanent compaction of fine-grained and clay sediment materials is considered more likely to lead to inelastic storativity.

3.3.2. Estimation of storage loss

The total volumetric variation in water in an aquifer system due to hydraulic head decline can be estimated from InSAR measurements (Fetter, 2000):

$$\Delta V = S_{sk} \times \Delta h \times A = \Delta b_{total} \times A \tag{6}$$

where Δb_{total} is the total InSAR deformation at a specific period and A is the aquifer area. GWS loss is equivalent to the cumulative compaction volume of a confined aquifer system, and it can also be, according to this formula, approximately equal to the cumulative land deformation volume estimated from InSAR measurements. To estimate the aquifer properties across the entire basin scale, sparse values were interpolated over a grid of 3 km × 3 km resolution using an inverse distance algorithm.

4. Results

4.1. Spatiotemporal InSAR results

According to the aforementioned InSAR-processing method, the spatiotemporal land deformation measurements were determined at an unprecedented spatial resolution across the Willcox Basin. Fig. 3 shows three average deformation rate maps in the LOS generated from ascending and descending Sentinel-1 and ascending ALOS-1 datasets. Two main subsidence zones were identified: the FGR land subsidence zone in the northern Willcox playa and the KS subsidence zone in the southern playa (Fig. 3d). The two narrow belt-shaped subsidence features along the margin of the basin connect the FGR and KS subsidence zones. A consistent spatial deformation pattern occurred from 2006 to 2020, while the deformation magnitude varied with time.

According to the rate maps, we observed an increasing trend of the deformation rate at both subsidence centres from the first (2006–2011) to the second (2016–2020) measurement periods. The ascending ALOS-1 LOS velocity map (Fig. 3c) illustrates that the highest subsidence occurred in the western KS subsidence zone with a maximum subsidence rate exceeding −8 cm/year, while Fig. 3a and b shows that the greatest subsidence occurred in the FGR subsidence zone with a maximum rate exceeding −14 cm/year.

Additionally, to develop a better understanding of the 2-D deformation characteristics, LOS displacement time series and velocity fields were decomposed into vertical and east-west components following the approach detailed in Section 3 by combining observations from Sentinel-1 ascending and descending viewing geometries. The north-south component of the displacement field is unresolvable, as both the ALOS-1 and Sentinel-1 satellites are in near-polar orbits; hence, the LOS geometry is insensitive to north-south motion. We could therefore calculate displacement time series in the vertical and east-west directions based on the satellite heading and LOS incidence angles for SAR acquisitions. Fig. 4a and b illustrates the vertical and horizontal deformation patterns during 2016–2020, respectively. Slight east-west deformation was observed: the western region moved westward with a

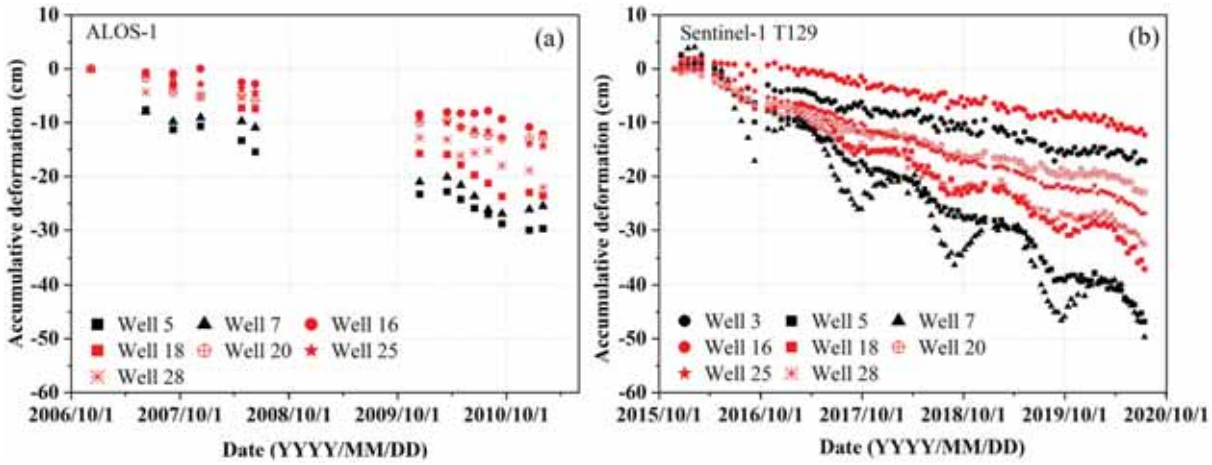

Fig. 5. Cumulative deformation time series at several typical observation wells: (a) ALOS-1; and (b) Sentinel-1 T129. Black symbols indicate the time series in the upper subsidence region, while red symbols indicate the time series in the lower subsidence region. Different symbols are used to distinguish time series at each well. The locations of these wells are indicated in Fig. 3a. (For interpretation of the references to colour in this figure legend, the reader is referred to the web version of this article.)

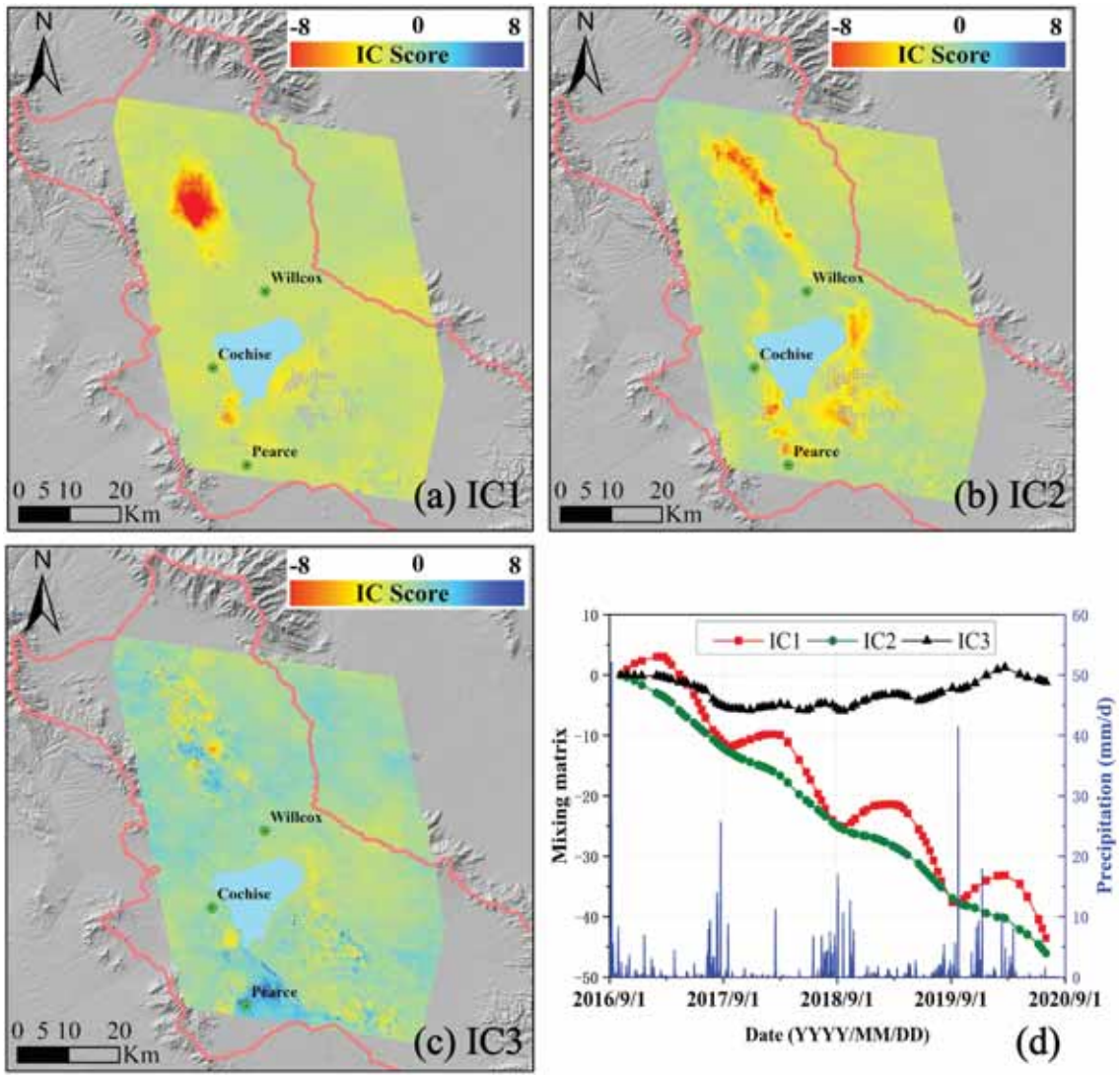

Fig. 6. ICA of InSAR data. (a-c) Independent component score maps scaled by the total contribution of the components retained from the original data: (a) IC1; (b) IC2; and (c) IC3. (d) Mixing matrix for the first three independent components. Negative score map values correspond to subsidence and negative mixing matrix values and vice versa.

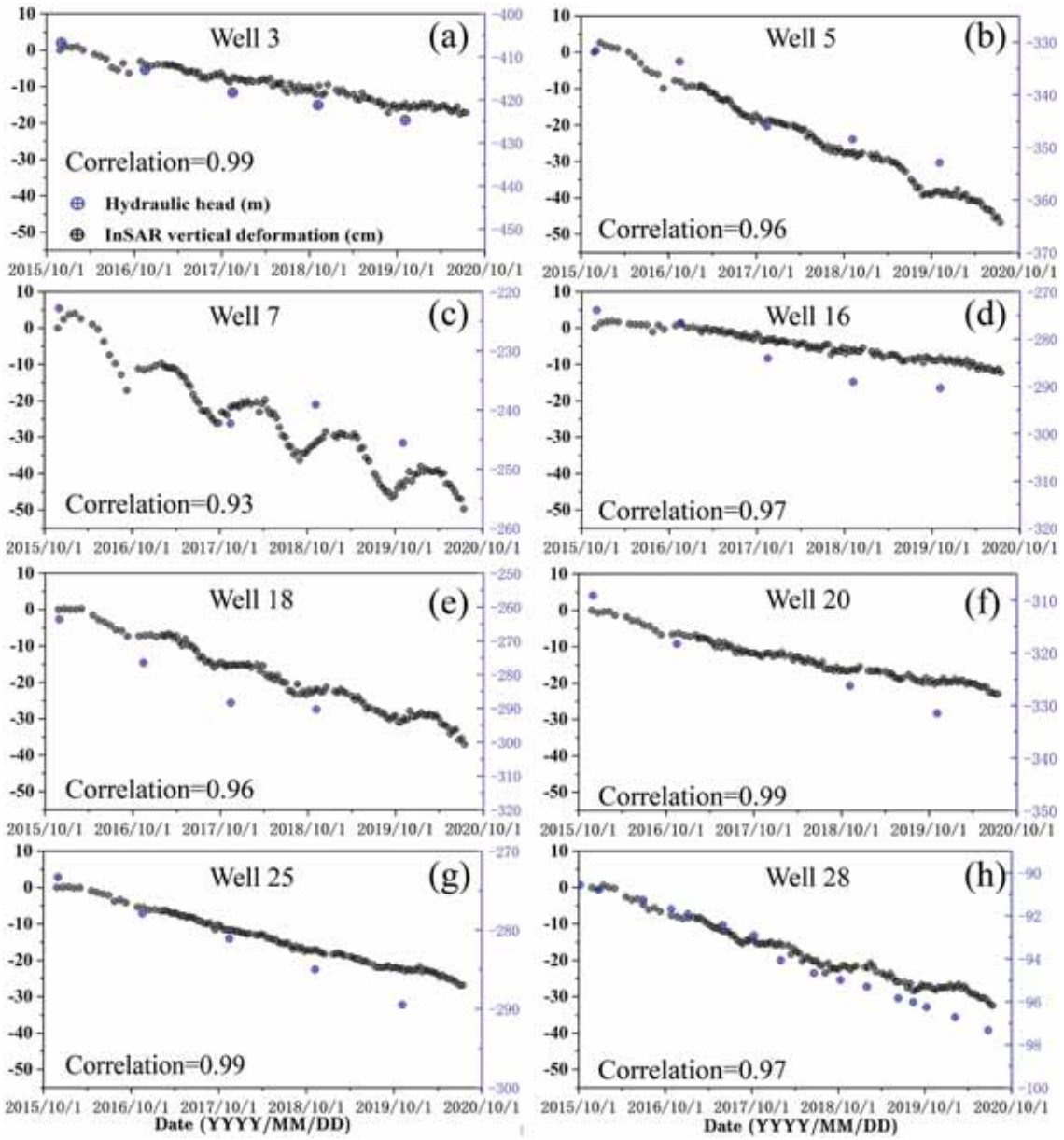

Fig. 7. Vertical InSAR deformation in comparison with hydraulic heads at eight observation wells. The blue dots show the groundwater level measurements in metres. The black dots show the InSAR deformation time series in centimetres. (For interpretation of the references to colour in this figure legend, the reader is referred to the web version of this article.)

positive value denoted by a blue colour, and the eastern region moved eastward with a negative value denoted by a green colour. We are primarily concerned with the vertical deformation of the basin in the following analysis.

To fully investigate the temporal evolution during the measurement periods, time series analysis of several typical wells was performed. The cumulative deformation at each typical observation well along the vertical direction is illustrated in Fig. 5. The typical points we chose were located in two different subsidence regions: well 3, well 5 and well 7 were in the upper FGR zone, and the remaining points were in the lower KS subsidence zone. In addition, these points were located in places possessing different spatiotemporal deformation features. For example, well 3 was located where the ground surface subsided almost linearly, but observations at well 7 showed subsidence with significant seasonality.

4.2. ICA decomposition of InSAR deformation

Through the use of ICA, different spatiotemporal deformation patterns of interest embedded in the InSAR land deformation time series could be isolated without any a priori information about latent signal sources. In this case, 117 SAR acquisitions were retained, where each had 5,506,866 pixels. Therefore, the observed matrix of InSAR time series O had a 117-by-5,506,866 dimension. First, PCA was explored to reduce data dimensionality. The first three principal components accounted for 99.18%, whereas the fourth component accounted for only 0.12%. Based on the PCA, the first three principal components accounting for 98%, 0.8%, and 0.4% of the data variance were retained for the following ICA. Therefore, what the following ICA revealed was the independent three features represented by the first three PCs.

Fig. 6 summarizes the spatial distribution of each component and the mixing matrix time series of each retained IC, demonstrating that ICA could identify and estimate the major spatial features and temporal

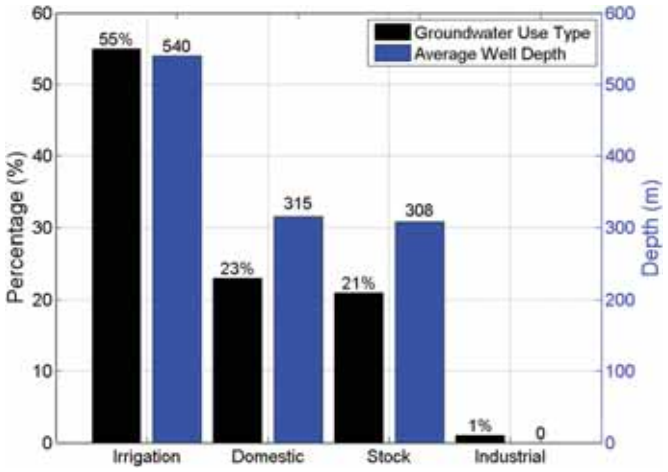

Fig. 8. The groundwater usage types and average well depth distribution of the observation wells in the Willcox Basin.

trends underlying the time series deformation. A score map (Fig. 6a-6c) shows that the pixels experienced the same time series trend, while the mixing matrix map (Fig. 6d) shows how much this independent component contributed at each acquisition time. By inspecting the component map pattern and the mixing matrix time series, it is easy to identify that IC1 and IC2 are dominated by long-term land subsidence deformation, and IC3 represents most residual contributions, including the residual turbulent delay and other noise. IC1 describes long-term subsidence accompanied by seasonal rebound throughout the observation period, while IC2 displays a nearly linear deformation trend over time with insignificant seasonal variability.

In the northern FGR subsidence region, IC1 recovers the central deformation pattern of all deformation characteristics, while the spatial extent of IC2 plots outside the IC1 deformation pattern. In the southern KS subsidence region, the deformation pattern is dominated by IC2 with nearly linear subsidence, and season-modulated long-term deformation mainly occurs in the area between the Cochise and Pearce communities.

4.3. Surface deformation in response to groundwater level

To investigate the correlation between groundwater level and surface deformation, we collected 48 water discharge time series datasets in the Willcox Basin. Fig. 7 illustrates the vertical deformation time series versus changes in groundwater at eight selected typical well locations (white dots in Fig. 3a). The trend of the InSAR time series is in accordance with that of the groundwater level, producing a strong positive correlation ($\geq$0.93) between the subsidence and groundwater level drawdown.

In addition, groundwater in the Willcox Basin is greatly exploited for agricultural irrigation, which accounts for 55%, and domestic and stock uses account for the remaining 44% (Fig. 8). Fig. 8 shows that the average hydraulic head depth, regardless of agricultural irrigation or other usages, is greater than 300 m. This suggests that subsidence in this basin is a result of human-induced compaction of sediments due to massive pumping in the deep aquifer system and groundwater depletion. Therefore, the measured InSAR deformation here is related to the compaction of the confined system, and the upper unconfined system does not contribute to land subsidence.

4.4. Aquifer system parameters/properties

4.4.1. Skeletal storativity

Hydraulic head levels represent the changes in groundwater level in a confined aquifer system (Δh), and InSAR data provide the total sediment compaction (Δb) over the aquifer's entire thickness. During the 2016–2020 period, the vertical compaction of the confined aquifer was determined from the refined InSAR observations after using the MSBAS and ICA methods. During the 2006–2011 period, it should be noted that only one ascending track of the ALOS-1 SAR image was acquired, thus the vertical compaction we used for the following analysis is the isolated deformation component from vertical deformation transformed from LOS deformation using the local incidence angles. Spatial storage coefficient maps at two observation periods were calculated by analysing the

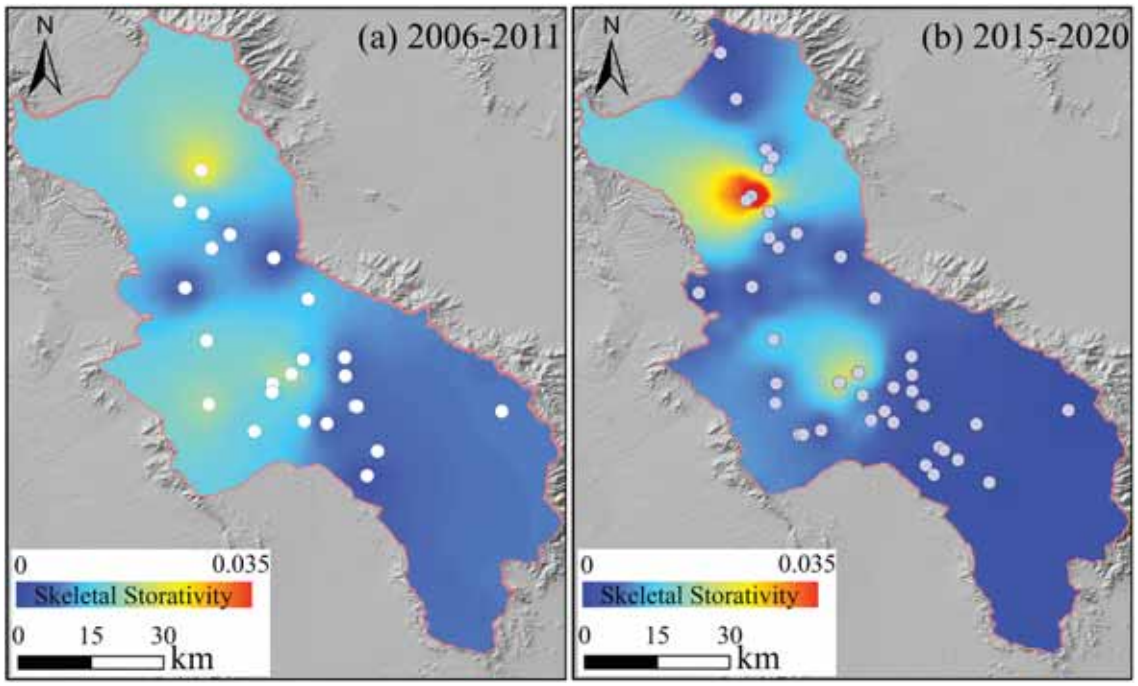

Fig. 9. Spatial distribution of average skeletal storativity obtained from contemporaneous measurements of water level and InSAR time series during (a) 2006 to 2011 and (b) 2015 to 2020.

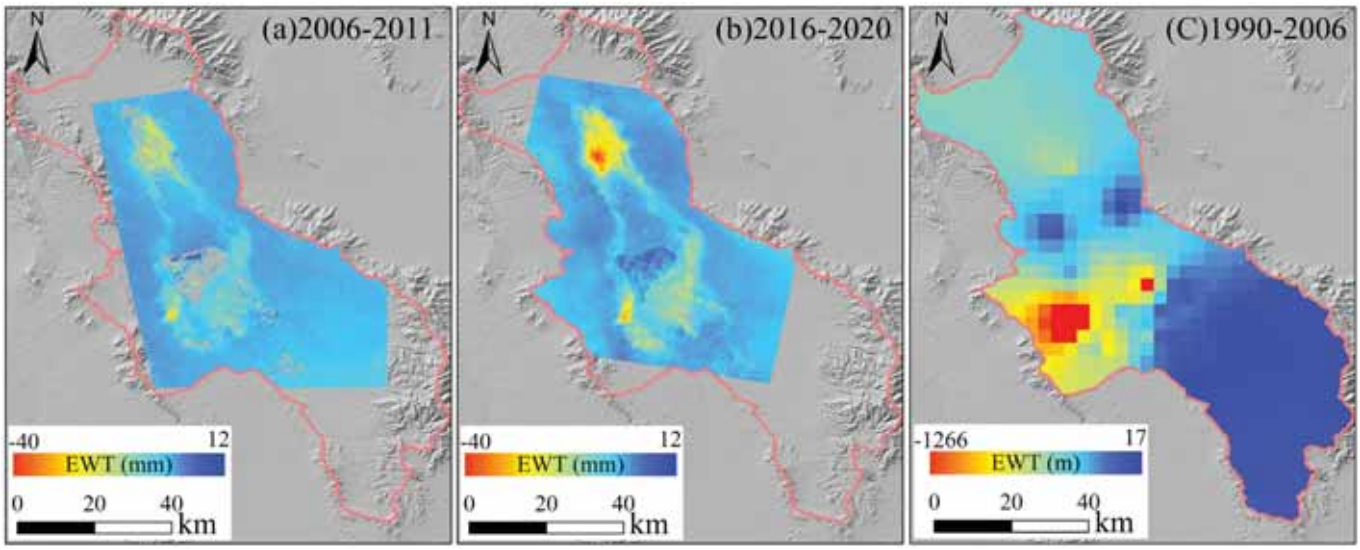

Fig. 10. Spatial distribution of groundwater storage variations: (a) average annual storage variations from 2006 to 2011, (b) average annual storage variations from 2016 to 2020, and (c) estimated cumulative groundwater storage loss from 1990 to 2006. The unit in the maps is equivalent water thickness (EWT).

relationship between the InSAR deformation time series and contemporaneous groundwater level measurements at several observation wells marked with white-filled circles using a least-squares inversion technique (Fig. 9). There was a wide variation in the estimated coefficients, ranging from 6.0×10^{-4} to 0.02 during 2006 to 2011 with an average of 0.008 and from 2.3×10^{-5} to 0.087 during 2015 to 2020 with an average of 0.005. This change indicates that the storage capacity of the confined aquifer system declined with the continuous exploitation of groundwater and compaction of the aquifer layer.

4.4.2. Groundwater storage loss

Permanent loss of aquifer storage of groundwater due to inelastic compaction poses a threat to groundwater availability now and in the future even if groundwater pumping is reduced. According to Eq. (6), the cumulative land deformation volume is approximately equivalent to the GWS variation in a confined aquifer system. Therefore, we utilize InSAR-derived deformation observations to estimate the spatiotemporal GWS variations in the Willcox Basin in the past two periods (2016–2020 and 2006–2011). Fig. 10a and Fig. 10b demonstrate the average annual GWS variations derived from the contemporaneous measurements of the water level and InSAR velocity. The estimated annual GWS was 2.6×10^7 m^3/year during 2006–2011 and 5×10^7 m^3/year during 2016–2020. The USGS also estimated groundwater withdrawals in the Willcox Basin from 1940 to 2014 (ADWR, 2018). Our estimated average groundwater loss in our observation period was underestimated compared with the 18×10^7 m^3/year estimated by the USGS (ADWR, 2018). This could probably be explained by the following reasons: 1) the USGS estimated the GWS in a wider range, while we only calculated the GWS underlying the area covered by the InSAR deformation; 2) the USGS surveyed the GWS of the entire aquifer system, including the upper unconfined aquifer, while the contribution of the GWS derived from InSAR was from confined aquifers and aquitards; and 3) GWS calculated from InSAR measurements included groundwater recharge, but that of the USGS did not.

Historical cumulative GWS depletion from 1990 to 2006 could be determined using the historical hydraulic head below the preconsolidation head and the estimated skeletal storativity according to Eq. 6 (Fig. 10c). The estimated cumulative GWS depletion was 3.7×10^8 m^3 from 1990 to 2006, which is consistent with that derived from the USGS in terms of magnitude (1.4×10^8 m^3). This consistency demonstrates that the accuracy of the estimated aquifer coefficients is reliable. Moreover, the dispersion and uncertainty are mainly related to interpolation errors as a result of sparse hydraulic head data.

5. Discussion

5.1. Land subsidence and earth fissures

Earth fissures are long and narrow soil tension cracks, which are generally caused by differential land subsidence (Conway, 2016). Earth fissures are widespread over the Willcox Basin due to long-term regional land subsidence associated with excessive exploitation of groundwater (Fig. 1a). Subsidence-related earth fissures are primarily found in areas of varying alluvium thickness over the margin of the groundwater basin or shallow bedrock near the Sulphur Hills (Figs. 1a and 3b). From the InSAR survey, we observed that there was relatively less subsidence along the basin margin (thinner alluvium) than along the central part of the basin (thicker alluvium), the result of which was the uneven compaction of different aquitard materials between the two sides of the basin margin (Figs. 1c and 3b). In the process of differential compaction, tension stretched the sediment until fissures developed.

5.2. PCA and ICA results

PCA was applied on the centred InSAR time series as the preconditioning of ICA processing. Three principal components were obtained by calculating the centred matrix eigenvalues and eigenvectors, which allowed the obtaining of lower dimensional data and preserved as many source signal features as possible. Fig. 11 shows the results of PCA on the vertical InSAR deformation derived from Sentinel-1A T129 datasets across the Willcox Basin, where Fig. 11a-11c illustrates the spatial patterns of the principal component score maps.

Despite the fact that three principal components captured major characteristics of the input-mixed InSAR signals, including the long-term deformation, seasonal fluctuation and noise, the contributions to each independent component came from all three sources. However, the decomposed signal is not in a set of statistically independent components. For example, all three signals contain the seasonal motion observed from the eigenvector time series (Fig. 11d). However, the results of ICA are more likely to represent independent sources since PCA maximizes signal variance rather than statistical independence when retrieving signal sources compared with ICA. Thus, ICA can be used to extract low magnitude signals without requiring any a priori assumptions beyond the independence of the components, even when there is a

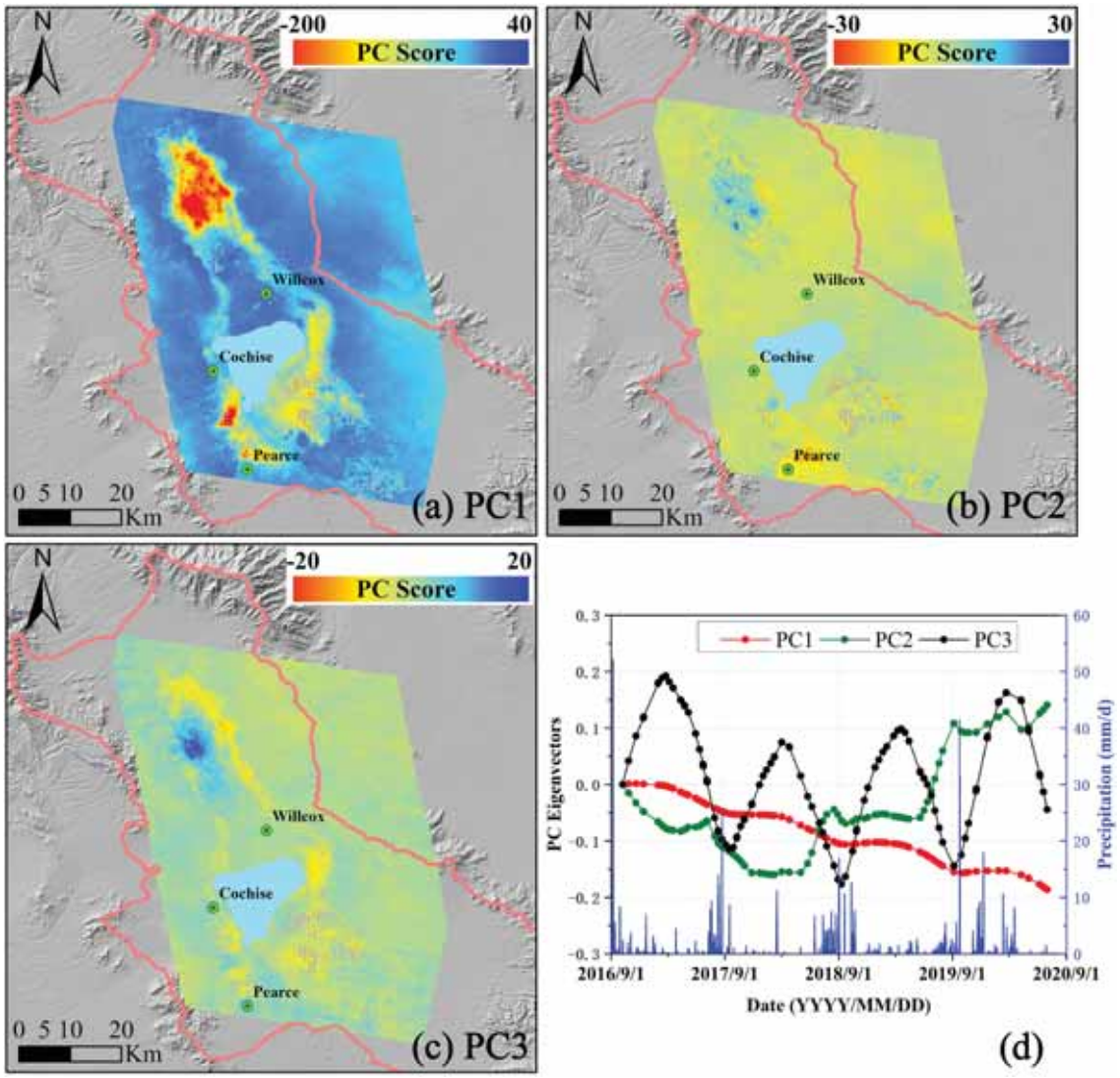

Fig. 11. PCA of vertical InSAR deformation. (a-c) Score maps of each PC: (a) PC1; (b) PC2; and (c) PC3. (d) Temporal eigenvector time series for the first three principal components.

high level of noise (Ebmeier, 2016; Hyvärinen and Oja, 2000). Additionally, unlike PCA, ICA decomposition was carried out in orthogonal space by utilizing centering and whitening techniques. After decomposition, the sign, magnitude and serial numbers of each independent component were ambiguous, as they were given in random order and the number order had no particular significance.

In addition, the aforementioned ICA outcomes revealed that the two types of spatiotemporal deformation characteristics exhibit both upper and lower subsidence zones. In the Willcox Basin, mountain front runoff is the primary recharge source of groundwater in the basin (Towne and Freark, 2001). On the one hand, under the control of topography, the runoff in each gully seeps into the local low-lying areas from the surrounding watershed along the terrain (Fig. 1b). Aquifer systems of low-lying areas can be more adequately recharged with seasonal runoff compared with the surrounding aquifers. On the other hand, the hydrogeological properties of aquifer systems are spatially variable, with heterogeneous clay and sand interlayers in deformation areas on the IC1 score map and homogeneous streaks of clay and sand units on the IC2 deformation score map (Fig. 1c). These results might explain why the seasonal amplitude in the IC1 score map is larger than that in the IC2 score map.

5.3. *Effect of ICA in improving InSAR time series*

Another main advantage of using ICA is improvement in the InSAR time series, which in turn can help to refine the time series for estimating hydrological parameters. After ICA processing, multiplying the component score with the mixing matrix allows retrieving the corresponding deformation time series history of each component. Therefore, the combination of IC1 and IC2 components returns the deformation time series, which is achieved by removing the residual noise represented by IC3.

Here, an example is presented showing how the residual error is corrected with the ICA method (Fig. 12). Significant turbulent delay occurred at the acquisition of 2019/06/02, affecting the quality of the interferograms constructed with the image acquired on this date. This was concluded by checking all interferograms constructed with this image, and then a similar effect was found in all of them. The original interferogram 2019/06/02–2019/07/20 is shown in Fig. 12a, where elevation-dependent atmospheric delay was removed. In this case, the error is mainly caused by turbulent atmospheric delay. The interferogram retrieved from time series analysis has no significant difference compared with the original interferogram (Fig. 12b). Fig. 12 (d-e) shows the separated IC3 score maps at acquisitions of 2019/06/02 and 2019/

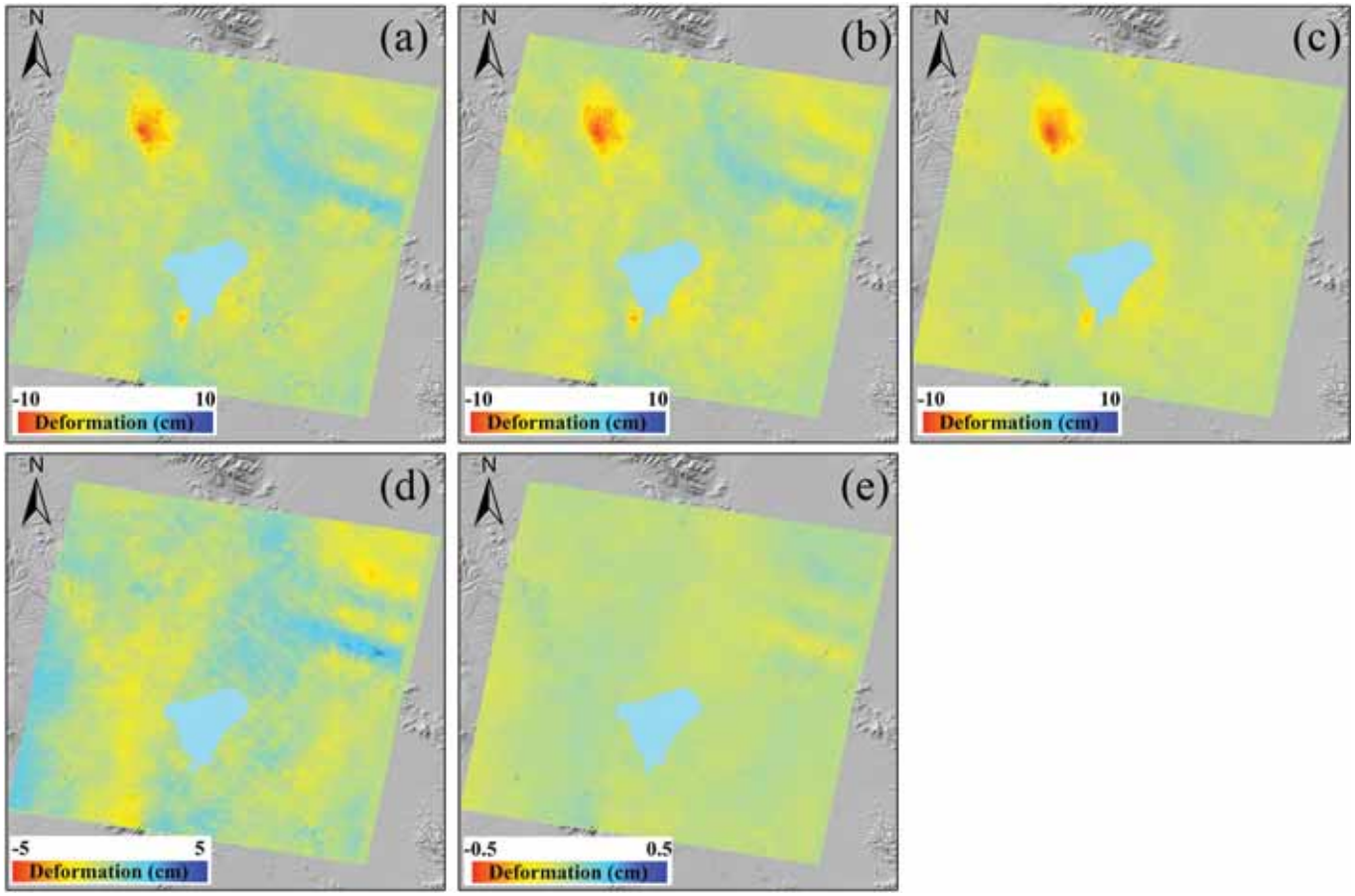

Fig. 12. Examples of the interferogram 2019/06/02–2019/07/20 before and after residual error correction using ICA. (a) Original unwrapped interferogram. (b) Interferogram retrieved from the time series. (c) Unwrapped interferogram reconstructed from IC1 and IC2. (d-e) IC3 components of 2019/06/02 and 2019/07/20.

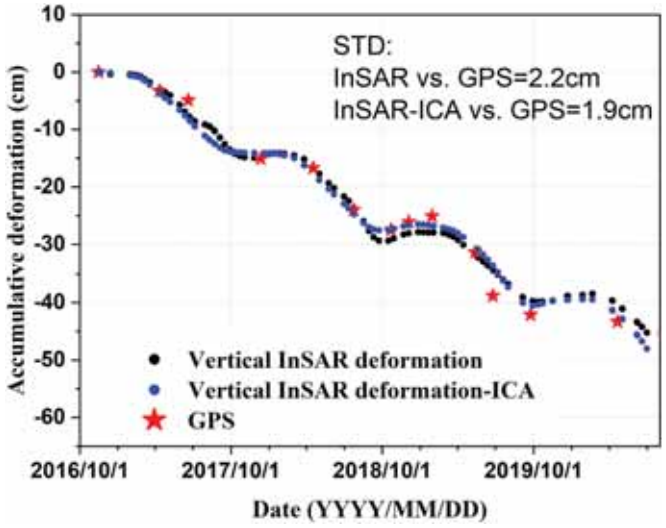

Fig. 13. Comparison of the vertical component of the GPS time series to the InSAR vertical component derived from Sentinel-1 (black dots) and the separated deformation component from IC analysis (blue dots). (For interpretation of the references to colour in this figure legend, the reader is referred to the web version of this article.)

07/20, indicating a highly similar spatial pattern to the turbulent atmospheric delay in Fig. 12a. The magnitude of the IC3 score map on image 2019/06/02 is more than 10 times as large as that on image 2019/07/20. Fig. 12c shows the final corrected interferogram after using the ICA method. This suggests that the major residual atmospheric signal in this interferogram was successfully mitigated and that ICA can be used as an effective method to mitigate error signals.

Additionally, the InSAR results were compared with the GPS observations to assess their accuracy. The observation period of the GPS station was from 2016 to 2020; therefore, the accuracy assessment was exploited only within this period, which was covered by the Sentinel-1 dataset. To further validate the accuracy of the observed deformation, the vertical component retrieved from 2-D analysis and the one obtained by separating deformation components from ICA were compared with the GPS time series. As illustrated in Fig. 13, the standard deviation of the latter is 13% lower than that of the former, indicating that the ICA improved the monitoring accuracy. Despite this, the standard deviation is still high, which is due to the lower accuracy (cm-level) of the GPS.

5.4. Elasticity vs. inelasticity skeletal storativity

The history of groundwater depletion across the Willcox Basin can be generalized into five stages on the basis of the pumpage: initial exploitation stage (before 1940), dramatic withdrawal stage (1940 to mid-1960s), withdrawal peak stage (late 1960s to mid-1970s), significant decreasing stage (early 1980s to 1990s), and increasing again stage (after1990s) (ADWR, 2018). Historical water table time series at 32 observation wells in the Willcox Basin can be traced back to the 1990s and even earlier, and we chose eight to display in Fig. 14.

According to the pumping history of available hydraulic data, we next assessed whether the land subsidence observed in the Willcox Basin was recoverable (elastic) or irrecoverable (inelastic). If the effective

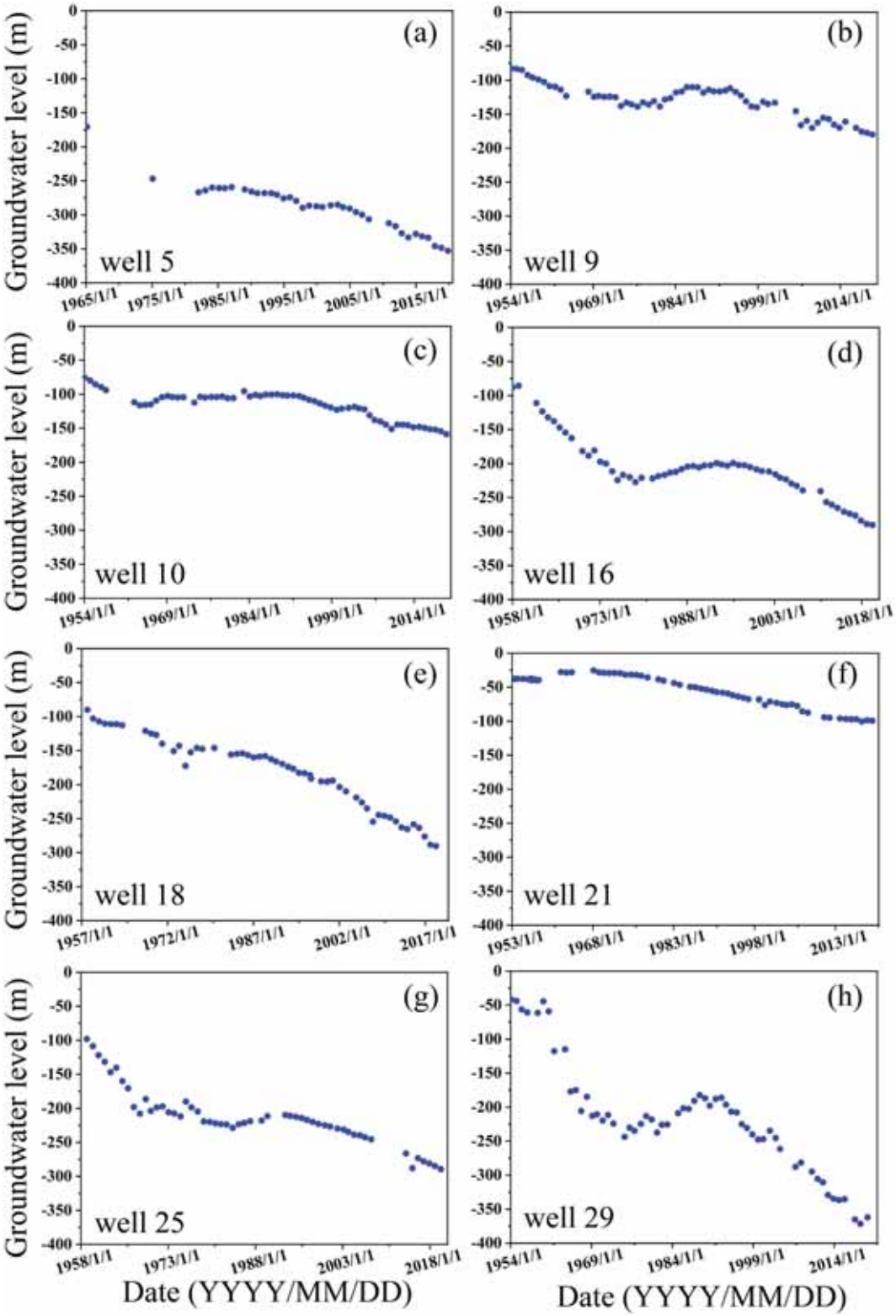

Fig. 14. Historical head measurements.

stress caused by groundwater decline exceeds the previous maximum stress, the aquifer system may likely undergo inelastic (i.e., permanent) compaction due to the consolidation of aquitards. The water table curves of wells are dominated by a clearly declining trend for more than three decades, with no signs of major recovery (Fig. 14). The preconsolidation head, defined as the highest groundwater level in most wells during the previous 1990–2020 depletion period, was the water table around the earlier 1990s (Fig. 14). Therefore, the pumping-induced subsidence from intensive compaction of fine-grained sand and clay-rich aquitards during a prolonged draining process suggests that quasi-irreversible compaction of the aquifer system has probably dominated the deformation field in the Willcox Basin since the 1990s, which is indicated by

the large number of earth fissures and cracks (Figs. 1a and 3b). Furthermore, this conclusion can also be reached based on our estimated storativity, since inelastic/irreversible deformation may arise when the skeletal storativity exceeds 0.005 (Fetter, 2000).

Since unconsolidated sand in aquifers normally does not compact inelastically, elastic deformation always occurs in the aquifer system regardless of whether the hydraulic head is below the preconsolidation head (highest head) (Smith et al., 2017). In the Willcox Basin, ICA has revealed two deformation patterns: long-term quasi-linear compaction and long-term compaction with season-modulated deformation, indicating that seasonal pore water pressure rebound occurred during the entire historical subsidence process. Based on InSAR time series measurements, the only clear elastic deformation we could observe in this region was the rapid response of surface deformation to seasonal variations in groundwater. In terms of surface deformation, seasonal deformation occurred in the centre of the northern FGR subsidence region and Cochise from the separated InSAR deformation measurements (Fig. 6a). However, we cannot conclude that seasonal elastic deformation occurred only in the area characterized by the IC1 score map. The spatiotemporal deformation feature represented by the IC2 score map also contains some elastic components, although at a lower amplitude compared with the IC1 score map. Additionally, the deformation amplitude of seasonal elastic deformation ranged from ± 2 cm to ± 6 cm, with the elastic/inelastic ratio tending to be close to zero, which was insignificant compared with the long-term compaction. Due to the lower sample frequency groundwater level at this well, observable seasonal recharge/discharge cycle information of the aquifer system could not be captured (Fig. 14). Based on this, the calculation of elastic and inelastic skeletal storativity was thus not distinguished in this research. If monthly/seasonally gathered water level records are available for this region, the map of aquifer hydrogeological properties can be further enhanced, such as by showing the separation of elastic and inelastic skeletal storativity.

6. Conclusions

Using the multitemporal InSAR technique and SAR data from the ALOS-1 and Sentinel-1 satellites, we investigated and analyzed the land deformation of the Willcox Basin in Arizona over two observation intervals (2006–2011 and 2015–2020). Multisensor InSAR time series analyses revealed two subsidence centres, FGR and KS, and showed the underlying spatiotemporal patterns of land subsidence. Since 2006, subsidence rates temporally increased, from a maximum of 8 cm/year to more than 14 cm/year, while the extent of the subsidence area spatially remained approximately the same. Subsidence was highly correlated with groundwater level declines in the deep confined aquifer, indicating that groundwater depletion for agricultural irrigation was the dominant influencing factor for surface deformation.

Using ICA, InSAR time series were spatiotemporally separated without any prior information to three independent components, including two deformation components and one noise component. After removing the noise, the application of ICA could improve the deformation accuracy by more than 13%. The different subsidence components unveiled different geomechanical processes around the subsidence zones.

Our study also demonstrated that a combination of InSAR and hydraulic data could estimate the storage coefficients of an aquifer system and GWS loss at a basin-wide scale. The estimated storage coefficients, ranging from 6.0×10^{-4} to 0.02 during 2006–2011 and from 2.3×10^{-5} to 0.087 during 2015–2020, signify an irreversible and unrecoverable deformation of the aquifer system in the Willcox Basin. The reduced average storage coefficient (from 0.008 to 0.005) indicates that long-term overdraft has already degraded the storage ability of the aquifer system and that groundwater pumping activities are unsustainable in the Willcox Basin.

InSAR can measure groundwater-induced surface deformation over a large-scale area, which can be utilized in groundwater flow models to refine hydraulic properties. Even though setting up a groundwater flow model is beyond the scope of this paper, the application of InSAR to quantify aquifer system properties through groundwater modelling is a frontier topic. We believe that the combination of this model with InSAR measurements will better guide water resource management to assess the mechanical health of aquifer systems across a large-scale aquifer system (Yeh et al., 2008).

Credit author statement

Mimi Peng: Methodology, Formal analysis, Funding acquisition, Writing, Review and Editing; Zhong Lu: Conceptualization, Supervision, Reviewing and Editing; Chaoying Zhao, Mahdi Motagh: Supervision, Reviewing and Editing; Lin Bai, Brian D. Conway, Hengyi Chen: Resources and Reviewing.

Declaration of Competing Interest

The authors declare that they have no known competing financial interests or personal relationships that could have appeared to influence the work reported in this paper.

Acknowledgements

The authors would like to thank the European Space Agency for providing the Sentinel-1 SAR data freely. ALOS/PALSAR data were copyrighted by Japan Aerospace Exploration Agency (JAXA). NASA's 1-arcsec global SRTM digital surface model was provided by USGS via Earth Explorer (https://earth explorer.usgs.gov). The hydraulic head and GPS data are provided by The Arizona Department of Water Resources (https://new.azwater.gov/). Shapefiles in Fig. 1 are courtesy of ADWR. The Arizona Geological Survey (AZGS) provides the related geological information. Constructive comments from Associate Editor and 4 anonymous reviewers improved the manuscript.

This research is jointly supported by the Natural Science Foundation of China (Grants No. 41874005, 41929001), the Fundamental Research Funds for the Central Universities, CHD (No. 300102269722, 300102269303) and the China Scholarship Council (No. 202006560072).

References

ADWR (Arizona Department of Water Resources), 2015a. Groundwater Sites Inventory (GWSI). https://gisweb.azwater.gov/waterresourcedata/GWSI.aspx. Accessed 5 February 2015.

ADWR (Arizona Department of Water Resources), 2015b. Land Subsidence Maps. http://www.azwater.gov/AzDWR/Hydrology/Geophysics/LandSubsidenceInArizona.html. Accessed 5 February 2015.

ADWR (Arizona Department of Water Resources), 2018. Groundwater Flow Model of the Willcox Basin. https://new.azwater.gov/hydrology/groundwater-modeling/willcox-model. Accessed 16 July 2018.

Amelung, F., Galloway, D.L., Bell, J.W., Zebker, H.A., Laczniak, R.J., 1999. Sensing the ups and downs of Las Vegas: InSAR reveals structural control of land subsidence and aquifer-system deformation. Geology 27, 483–486.

Berardino, P., Fornaro, G., Lanari, R., Sansosti, E., 2002. A new algorithm for surface deformation monitoring based on small baseline differential SAR interferograms. IEEE Trans. Geosci. Remote Sens. 40, 2375–2383.

Blackwell, E., Shirzaei, M., Ojha, C., Werth, S., 2020. Tracking California's sinking coast from space: Implications for relative sea-level rise. Sci. Adv. 6.

Bonì, R., Pilla, G., Meisina, C., 2016. Methodology for detection and interpretation of ground motion areas with the A-DInSAR time series analysis. Remote Sens. 8, 686.

Chaussard, E., Farr, T.G., 2019. A new method for isolating elastic from inelastic deformation in aquifer systems: application to the San Joaquin Valley, CA. Geophys. Res. Lett. 46, 10800–10809.

Chaussard, E., Bürgmann, R., Shirzaei, M., Fielding, E.J., Baker, B., 2014. Predictability of hydraulic head changes and characterization of aquifer-system and fault properties from InSAR-derived ground deformation. J. Geophys. Res. Solid Earth 119, 6572–6590.

Chaussard, E., Milillo, P., Burgmann, R., Perissin, D., Fielding, E.J., Baker, B., 2017. Remote sensing of ground deformation for monitoring groundwater management practices: application to the Santa Clara Valley during the 2012-2015 California drought. J. Geophys. Res. Solid Earth 122, 8566–8582.

Chen, Y., Tan, K., Yan, S., Zhang, K., Zhang, H., Liu, X., Li, H., Sun, Y., 2019. Monitoring land surface displacement over Xuzhou (China) in 2015-2018 through PCA-based correction applied to SAR interferometry. Remote Sens. 11, 1494.
Chen, B., Gong, H., Chen, Y., Li, X., Zhou, C., Lei, K., Zhu, L., Duan, L., Zhao, X., 2020. Land subsidence and its relation with groundwater aquifers in Beijing Plain of China. Sci. Total Environ. 735, 13911.
Cigna, F., Tapete, D., 2021. Present-day land subsidence rates, surface faulting hazard and risk in Mexico City with 2014–2020 Sentinel-1 IW InSAR. Remote Sens. Environ. 253.
Cohen-Waeber, J., Burgmann, R., Chaussard, E., Giannico, C., Ferretti, A., 2018. Spatiotemporal patterns of precipitation-modulated landslide deformation from independent component analysis of InSAR time series. Geophys. Res. Lett. 45, 1878–1887.
Conway, B.D., 2016. Land subsidence and earth fissures in south-central and southern Arizona, USA. Hydrogeol. J. 24, 649–655.
De Zan, F., Monti Guarnieri, A., 2006. TOPSAR: terrain observation by progressive scans. IEEE Trans. Geosci. Remote Sens. 44, 2352–2360.
Ebmeier, S.K., 2016. Application of independent component analysis to multitemporal InSAR data with volcanic case studies. J. Geophys. Res. Solid Earth 121, 8970–8986.
Fetter, C., 2000. Applied Hydrogeology: International Edition, 4th ed.
Galloway, D.L., Burbey, T.J., 2011. Review: regional land subsidence accompanying groundwater extraction. Hydrogeol. J. 19, 1459–1486.
Ghosh, B., Motagh, M., Haghighi, M.H., Vassileva, M.S., Walter, T.R., Maghsudi, S., 2021. Automatic detection of volcanic unrest using blind source separation with a minimum spanning tree based stability analysis. IEEE J. Sel. Top. Appl. Earth Obs. Remote Sens. 14, 7771–7787.
Gootee, B., 2012. Geologic evaluation of the Willcox Basin for carbon dioxide sequestration. In: Arizona Geological Survey. Open-File Report OFR-12-03.
Gualandi, A., Liu, Z., 2021. Variational Bayesian independent component analysis for InSAR displacement time-series with application to central California, USA. J. Geophys. Res. Solid Earth 126 e2020JB020845.
Haghshenas-Haghighi, M., Motagh, M., 2019. Ground surface response to continuous compaction of aquifer system in Tehran, Iran: results from a long-term multi-sensor InSAR analysis. Remote Sens. Environ. 221, 534–550.
Hoffmann, J., Galloway, D.L., Zebker, H.A., 2003. Inverse modeling of interbed storage parameters using land subsidence observations, Antelope Valley, California. Water Resour. Res. 39, 1031.
Hyvärinen, A., 1999. Fast and robust fixed-point algorithms for independent component analysis. IEEE Trans. Neural Netw. 10, 626–634.
Hyvärinen, A., Oja, E., 2000. Independent component analysis: algorithms and applications. Neural Netw. 13, 411–430.
Jacob, C.E., 1950. Flow of groundwater. In: Engineering Hydraulics. John Wiley, New York, pp. 321–386.
Jiang, L., Bai, L., Zhao, Y., Cao, G., Wang, H., Sun, Q., 2018. Combining InSAR and hydraulic head measurements to estimate aquifer parameters and storage variations of confined aquifer system in Cangzhou, North China Plain. Water Resour. Res. 54, 8234–8252.
Kositsky, A.P., Avouac, J.P., 2010. Inverting geodetic time series with a principal component analysis-based inversion method. J. Geophys. Res. Solid Earth 115, B03401.
Lanari, R., Mora, O., Manunta, M., Mallorqui, J.J., Berardino, P., Sansosti, E., 2004. A small-baseline approach for investigating deformations on full-resolution differential SAR interferograms. IEEE Trans. Geosci. Remote Sens. 42, 1377–1386.
Liang, H.Y., Zhang, L., Lu, Z., Li, X., 2019. Nonparametric estimation of DEM error in multitemporal InSAR. IEEE Trans. Geosci. Remote Sens. 57, 10004–10014.
Lin, Y.-N., Kositsky, A.P., Avouac, J.-P., 2010. PCAIM joint inversion of InSAR and ground-based geodetic time series: application to monitoring magmatic inflation beneath the Long Valley Caldera. Geophys. Res. Lett. 37, L23301.
Liu, Y., Liu, J., Xia, X., Bi, H., Huang, H., Ding, R., Zhao, L., 2021. Land subsidence of the Yellow River Delta in China driven by river sediment compaction. Sci. Total Environ. 750, 142165.
Lu, Z., Danskin, W., 2001. InSAR analysis of natural recharge to define structure of a ground-water basin, San Bernardino, California. Geophys. Res. Lett. 28, 2661–2664.
Maubant, L., Pathier, E., Daout, S., Radiguet, M., Doin, M.P., Kazachkina, E., Kostoglodov, V., Cotte, N., Walpersdorf, A., 2020. Independent component analysis and parametric approach for source separation in InSAR time series at regional scale: application to the 2017-2018 slow slip event in Guerrero (Mexico). J. Geophys. Res. Solid Earth 125 e2019JB018187.
Miller, M.M., Shirzaei, M., 2015. Spatiotemporal characterization of land subsidence and uplift in Phoenix using InSAR time series and wavelet transforms. J. Geophys. Res. Solid Earth 120, 5822–5842.
Miller, M.M., Shirzaei, M., Argus, D., 2017. Aquifer mechanical properties and decelerated compaction in Tucson, Arizona. J. Geophys. Res. Solid Earth 122, 8402–8416.
Molan, Y.E., Lu, Z., 2020. Modeling InSAR phase and SAR intensity changes induced by soil moisture. IEEE Trans. Geosci. Remote Sens. 58, 4967–4975.
Motagh, M., Shamshiri, R., Haghshenas Haghighi, M., Wetzel, H.-U., Akbari, B., Nahavandchi, H., Roessner, S., Arabi, S., 2017. Quantifying groundwater exploitation induced subsidence in the Rafsanjan plain, southeastern Iran, using InSAR time-series and in situ measurements. Eng. Geol. 218, 134–151.
Oram, P.I.I.I., 1993. Maps showing groundwater conditions in the Willcox Basin Graham and Cochise counties, Arizona-1990. In: ADWR Hydrologic Map Series Report No. 25, 2 Sheets, Scale 1:250,000.
Peng, M., Zhao, C., Zhang, Q., Lu, Z., Li, Z., 2019. Research on spatiotemporal land deformation (2012-2018) over Xi'an, China, with multi-sensor SAR datasets. Remote Sens. 11, 664.
Peng, M., Zhao, C., Zhang, Q., Lu, Z., Bai, L., Bai, W., 2020. Multi-scale and multi-dimensional time series InSAR characterizing of surface deformation over Shandong Peninsula, China. Appl. Sci. 10, 2294.
Qu, F.F., Lu, Z., Zhang, Q., Bawden, G.W., Kim, J.W., Zhao, C.Y., Qu, W., 2015. Mapping ground deformation over Houston-Galveston, Texas using multi-temporal InSAR. Remote Sens. Environ. 169, 290–306.
Richard, S.M., Reynolds, S.J., Spencer, J.E., Pearthree, P.A., 2000. Geologic Map of Arizona: Arizona Geological Survey Map 35, 1 Sheet, Scale 1:1,000,000.
Samsonov, S.V., d'Oreye, N., 2017. Multidimensional Small Baseline Subset (MSBAS) for two-dimensional deformation analysis: case study Mexico City. Can. J. Remote. Sens. 43, 318–329.
Smith, R.G., Knight, R., Chen, J., Reeves, J.A., Zebker, H.A., Farr, T., Liu, Z., 2017. Estimating the permanent loss of groundwater storage in the southern San Joaquin Valley, California. Water Resour. Res. 53, 2133–2148.
Terzaghi, K., 1925. Principles of soil mechanics: IV. Settlement and consolidation of clay. Eng. News Rec. 95, 874–878.
Terzaghi, K., 1943. Theoretical Soil Mechanics. John Wiley, New York, p. 510.
Towne, D.C., Freark, M.C., 2001. Ambient Groundwater Quality of the Willcox Basin: A 1999 Baseline Study. ADEQ OFROl-09, Phoenix, AZ.
Vajedian, S., Motagh, M., 2019. Extracting sinkhole features from time-series of TerraSAR-X/TanDEM-X data. ISPRS J. Photogramm. Remote Sens. 150, 274–284.
Werner, C., Wegmüller, U., Strozzi, T., Wiesmann, A., 2000. GAMMA SAR and interferometric processing software. In: Proceedings of ERS - ENVISAT Symposium, Gothenburg, Sweden, vol. 1620.
Yeh, T.-C.J., Lee, C.-H., Hsu, K.-C., Illman, W.A., Barrash, W., Cai, X., Daniels, J., Sudicky, E., Wan, L., Li, G., Winter, C.L., 2008. A view toward the future of subsurface characterization: CAT scanning groundwater basins. Water Resour. Res. 44, W03301.